Journal of Catalysis 415 (2022) 77–86

Contents lists available at ScienceDirect

Journal of Catalysis

journal homepage: www.elsevier.com/locate/jcat

General strategy for enhanced CH_4 selectivity in photocatalytic CO_2 reduction reactions by surface oxophilicity engineering

Wenhao Li [b], De-Kun Ma [a,*], Xia Hu [c], Faliang Gou [a], Xiaogang Yang [d], Walker MacSwain [e], ChenZe Qi [a], Weiwei Zheng [e,*]

[a] Zhejiang Key Laboratory of Alternative Technologies for Fine Chemicals Process, Shaoxing University, Shaoxing 312000, China
[b] Zhejiang Key Laboratory of Carbon Materials, Wenzhou University, Wenzhou 325027, China
[c] School of Life Science, Shaoxing University, Shaoxing 312000, China
[d] Institute of Materials Science and Devices, Suzhou University of Science and Technology, Suzhou 215011, China
[e] Department of Chemistry, Syracuse University, Syracuse, NY 13244, USA

ARTICLE INFO

Article history:
Received 9 July 2022
Revised 2 October 2022
Accepted 5 October 2022
Available online 10 October 2022

Keywords:
Photocatalytic CO_2 reduction
Oxophilicity engineering
Doping
Selectivity
Methane

ABSTRACT

Rationally designing and controlling the interactions between reaction intermediates and the surface of photocatalysts is critical to obtain high product selectivity in photocatalysis. Herein, using CdS-based photocatalytic CO_2 reduction reaction (CO_2RR) as a model system, we demonstrate that CH_4 selectivity can be significantly enhanced through the introduction of La^{3+} ions with high oxophilicity on the surface of the photocatalysts. The high surface oxophilicity of the photocatalysts can increase CO^* desorption energy and promote further hydrogenation to CH_4. In contrast, when Au^{3+} ions with low oxophilicity were doped in CdS, reduced CH_4 selectivity was observed in the CO_2RR. Significantly, enhanced CH_4 selectivity can be achieved by doping oxophilic La^{3+} ions into a broad range of alternative photocatalysts including ZnO, SnS_2, BiOBr, $BiVO_4$, TaON, and $CsPbBr_3$, which demonstrates the general strategy to enhance CH_4 selectivity of photocatalytic CO_2RR through increased surface oxophilicity of the photocatalysts by rare earth La^{3+} ion doping.

© 2022 Elsevier Inc. All rights reserved.

1. Introduction

Photocatalytic CO_2RR for the generation of solar fuels represents one of the ideal sustainable technologies that can simultaneously overcome environmental issues and the energy crisis [1]. While photocatalytic activity and stability have been widely studied, the control of product selectivity of photocatalytic CO_2RR is challenging and less explored [2].The photocatalytic CO_2RR process usually involves proton-coupled multi-electron transfers and reaction process with various intermediate products which can be produced due to their similar reduction potentials [3]. Therefore, it is crucial to enhance product selectivity through manipulating the reaction pathways on the photocatalysts to reduce unnecessary separation costs [4]. So far, there have been several successful strategies for obtaining highly selective products of photocatalytic CO_2RR such as loading appropriate co-catalysts [5], rational fabrication of dual metal active sites [6], the introduction of O_2 [7], doping [8], and defect engineering [9]. However, most of the reported methods are specific to a certain photocatalytic system and a general method to refine product selectivity of photocatalytic CO_2RR is still lacking.

By tailoring the interactions of intermediates with active sites of a photocatalyst, high product selectivity can be achieved [10]. The oxophilicity of the catalyst surface is closely related to its binding affinity with oxygen [11]. Therefore, in principle, the product selectivity of catalytic reactions involving oxygen-containing intermediates can be adjusted through manipulating the oxophilicity of catalyst surface. Indeed, the importance of the surface oxophilicity of catalysts in organic synthetic chemistry has been reported back in the 1980s [12]. Recently, tailoring surface oxophilicity of a catalyst to obtain high product selectivity has received renewed interest. For example, the glycerol hydrodeoxygenation reaction selectivity can be tuned through modifying the surface cationic oxophilicity of Mo_2C with Cu [13].

Considering that most intermediates derived from photocatalytic CO_2RR are oxygen-containing species, we hypothesize that the corresponding product selectivity could be enhanced through controlling surface oxophilicity of photocatalysts. Usually, the main gaseous products of photocatalytic CO_2RR are CO and CH_4, which involves $2e^- + 2H^+$ and $8e^- + 8H^+$ processes, respectively. If the surface oxophilicity of a photocatalysts is enhanced, its binding

* Corresponding authors.
E-mail addresses: dkma@usx.edu.cn (D.-K. Ma), wzhen104@syr.edu (W. Zheng).

https://doi.org/10.1016/j.jcat.2022.10.004
0021-9517/© 2022 Elsevier Inc. All rights reserved.

ability to CO* will be increased, and therefore, boosted CH_4 selectivity could be achieved. To prove our hypothesis, we used CdS hierarchical microspheres (HMSs) for photocatalytic CO_2RR as a model system and doped strongly oxophilic La^{3+} ions on the CdS surface to enhance CH_4 selectivity. CdS is chosen mainly considering that it is a popular visible light-driven photocatalyst, which has been widely applied to photocatalytic CO_2RR [14]. So far, although various strategies have been developed to manipulate the product selectivity of CdS photocatalysts, the most commonly reported gaseous products are CO [15]. In addition, La^{3+} ion can be doped into CdS lattice [16], which provides a way to manipulate the oxophilicity of the CdS photocatalyst. As we expected, it was found that CH_4 selectivity was increased from 46 % to 74 % (product basis) and 77 % to 92 % (electron basis) after La^{3+} ions were introduced on the surface of CdS photocatalysts. More significantly, it was found that surface oxophilicity engineering by La^{3+} ion doping is a general strategy for enhanced CH_4 selectivity and can be applied to various photocatalysts including ZnO, SnS_2, BiOBr, $BiVO_4$, TaON, and $CsPbBr_3$. This work provides new insights on the surface engineering in tuning catalytic reaction selectivity for the design of highly selective photocatalysts for CO_2RR.

2. Experimental

2.1. Materials

Ethylenediamine ($C_2H_8N_2$) and nitric acid (HNO_3) were purchased from Zhejiang Zhongxing Chemical Co. Ltd. Hydrogen peroxide (H_2O_2) was supplied by Shanghai Union Chemical Co. Ltd. All other chemicals including cadmium acetate ($Cd(Ac)_2{\cdot}2H_2O$), thiourea (CH_4N_2S), zinc acetate ($Zn(CH_3COO)_2$), tantalum pentoxide (Ta_2O_5), lanthanum nitrate hexahydrate ($La(NO_3)_3{\cdot}6H_2O$), potassium bromide (KBr), bismuth nitrate pentahydrate ($Bi(NO_3)_3{\cdot}5H_2O$), sodium diethyldithiocarbamatre trihydrate ($(C_2H_5)_2NCSSNa{\cdot}3H_2O$), tin chloride pentahydrate ($SnCl_4{\cdot}5H_2O$), titanium dioxide (TiO_2), sodium metavanadate ($NaVO_3$), ethylenediamine tetraacetic acid (EDTA, $C_{10}H_{16}N_2O_8$), sodium hydroxide (NaOH), cesium bromide (CsBr), lead bromide ($PbBr_2$), N,N-dimethylformamide (DMF, $HCON(CH_3)_2$), chloroauric acid ($HAuCl_4$), ethylene glycol ($(CH_2OH)_2$), triethanolamine (TEOA, $C_6H_{15}NO_3$), and ethanol (C_2H_5OH) were purchased from Aladdin Shanghai Co. Ltd.

2.2. Syntheses of CdSHMSs and CdS:La^{3+} HMSs

Typically, 2.0 mmol of $Cd(OAc)_2{\cdot}2H_2O$ and 6.0 mmol of thiourea were dissolved into 30 mL of ethylenediamine under stirring. Then the solution was transferred to a Teflon-lined stainless-steel autoclave (50 mL), heated at 100 ℃ for 8 h. After it was cooled to room temperature, the yellow CdS powders were washed several times with deionized water and ethanol successively, and dried in an oven at 60 °C. For the synthesis of high-crystallinity CdS HMSs, the as-obtained CdS powders were further annealed at 500 °C under Ar for 2 h. CdS:La^{3+} HMSs were synthesized through an impregnation method. In a typical process, 0.5 mmol of CdS powders were added into 6 mL of $La(NO_3)_3{\cdot}6H_2O$ aqueous solution (2.5 mM) under stirring. Then the solution was dried at 100 °C. The resultant solid powders were further annealed at 500 °C under Ar for 2 h.

2.3. Characterization of materials

X-ray diffraction (XRD, D8 Advance) was used to characterize the crystal phases of the products. Field emission scanning electron microscopy (FE-SEM, Nova NanoSEM 200) and high-resolution transmission electron microscopy (HRTEM, JEOL 2010) coupled with energy-dispersive X-ray (EDX) spectroscopy were used to study the morphology and composition of the samples. UV–Vis absorption spectra (Shimadzu 2450) obtained by a diffuse reflectance spectroscopy with $BaSO_4$ as the reference for studying the optical responsive range of the samples. The inductively coupled plasma (ICP) optical emission spectroscopy (ICP-OES, America Agilent 725) was used to detect the actual doping concentration of La in CdS:La^{3+} HMSs. X-ray photoelectron spectroscopy (XPS, Escalab 250Xi, Thermo Scientific) was used to analyze the composition and chemical states of the prepared samples, using Al Kα radiation (hν = 1486.6 eV) as excitation. The ultraviolet photoelectron spectrum (UPS) was attached to the same XPS system to determine energy band position of the sample. N_2 adsorption–desorption isothermals were recorded on a Micromeritics ASAP2020 instrument, which was further used to measure specific surface area of the samples. CO_2 adsorption isotherms were measured at room temperature using the same apparatus. Photoluminscence (PL) spectra were measured on a Fluoromax-4 spectrofluorometer (HORIBA JobinYvon Inc.) under an excitation wavelength of 365 nm at room temperature. The electrochemical impendence spectra (EIS) were carried out at 1 V versus reversible hydrogen electrode with an amplitude of 5 mV in a frequency range from 0.1 MHz to 0.1 Hz in 0.5 M Na_2SO_4 electrolyte in the dark and under light irradiation (AM1.5G, 100 mW cm^{-2}). Photocurrent – time curves of the photoelectrodes were performed in 0.5 M Na_2SO_4 aqueous electrolyte under chopped light illumination (AM 1.5 G, 100 mW cm^{-2}). CO_2-temperature programmed desorption (CO_2-TPD) and CO-TPD were performed on a Quantachrome ChemBET Pulsar TPR/TPD automated chemisorption analyzer. Insitu diffuse reflectance infrared Fourier transform spectroscopy (DRIFTS) was performed on a Nicolet iS50 FTIR spectrometer (Thermo Scientific, USA). Before DRIFTS testing, the samples were pretreated at 423 K for 4 h. Then, CO_2 and H_2O gases were introduced into the IR cell loading the sample. The baseline was obtained after adsorption equilibrium of CO_2 on the sample for 20 min. Subsequently, light source (Perfect Microsolar 300 W Xe lamp equipped with a 420 nm cutoff filter) was turned on and DRIFTS spectra of the samples at different time intervals were recorded. The gaseous and liquid products from the photocatalytic CO_2RR were analyzed by gas chromatograph (Fuli GC9790) and ^1H NMR spectroscopy (Bruker, 500 M), respectively.

2.4. Photocatalytic CO_2RR

The photocatalytic CO_2RR was carried out in a closed reactor containing a quartz container. Typically, 10 mg of photocatalysts were dispersed into the mixed solvents of H_2O and TEOA (V_{water}: V_{TEOA} = 10:1). Then the reaction setup was alternately vacuum-degassed and purged with highly pure CO_2 for three times. The pressure of CO_2 in the reactor was kept at one atmosphere. A 300 W Xenon lamp equipped with a high-pass filter (λ > 420 nm) was utilized as the visible light source. The intensity of light source is adjusted to 300 mW/cm^2 and irradiated area is 11.3 cm^2. The reaction temperature was controlled at 15 ℃ by circulating cooling water coupled with a heater. The gaseous products were analyzed by a gas chromatography (Fuli GC9790). To evaluate the stability of photocatalysts, the photocatalytic CO_2RR was performed for 6 h at first. After that, 1 mL of TEOA was added to the quartz container to replenish the consumed part of TEOA before next cycle test. The processes were repeated five additional times.

2.5. Computational details

All the spin-polarized theoretical simulations in our work were performed on the Vienna ab initio Simulation Package (VASP) with the version 5.4.1 [17,18]. The generalized gradient approximation (GGA) with the Perdew-Burke-Emzerhof (PBE) functional form was used to evaluate the electron–electron exchange and correlation interactions while the projector augmented-wave (PAW) methods were implanted to represent the core-electron (valence electron) interactions [19–21]. Plane-Wave basis function was set with a kinetic cut-off energy of 550 eV. The ground-state atomic geometries were optimized by relaxing the force below 0.02 eV/Å and the convergence criteria for energy was set with the value of 1.0×10^{-5} eV/cell. The Brillouin zone was sampled using a Monkhorst-Pack meshes with $5 \times 5 \times 1$. Gaussian method was employed for both electronic structures and total energy of our models and stress/force relaxations. To better describe the interactions between molecules, van der Waal (vdw) interactions are included describing by DFT-D3 method of Grimme [22]. Free Energy under standard conditions (298 K) was calculated. Gibbs free Energy (ΔG) was computed by the equation of $\Delta G = \Delta E + \Delta EZPE - T\Delta S$, where the ΔE is the difference energy between each reaction step, $\Delta EZPE$ is the difference of the zero-point energy between each reaction step, ΔS is the difference of vibrational entropy between each reaction step.

3. Results and discussion

3.1. Characterization of CdS HMSs and La^{3+} ions doped CdS HMSs (CdS:La^{3+} HMSs)

The host CdS HMSs were synthesized through a solvothermal route and CdS:La^{3+} HMSs were synthesized by an impregnation method, respectively (See details in Experimental section). To simplify descriptions of experimental results, the doped sample with the highest photocatalytic activity and selectivity was screened out and used for subsequent study. As a result, the optimal doping concentration of La^{3+} ion is *ca.* 3 % (Fig. S1). The FE-SEM image of the CdS HMSs obtained through the solvothermal route indicates that the HMSs consist of the assembled nanosheets (Fig. S2). The XRD pattern of the sample could be indexed to hexagonal phase CdS (JCPDS no. 41–1049), even though its crystalline degree is relatively low (Fig. 1a). To improve the crystallinity of the products and promote efficient La^{3+} doping into CdS lattice, the as-synthesized CdS HMSs and CdS:La^{3+} HMSs were further treated at 500 °C under Ar atmosphere for two hours. The as-obtained CdS HMSs and CdS:La^{3+} HMSs after thermal annealing maintain their original morphology (Fig. 1b and Fig. 1c) but have higher crystallinity in hexagonal phase (Fig. 1a). As seen from their magnified XRD patterns (Fig. S3), FWHM (full width at half maximum) of the diffraction peaks for La^{3+} ions doped CdS HMSs are larger than those of undoped CdS HMSs, while diffraction peaks of CdS:La^{3+} HMSs shift to lower degree. According to Scherrer's equation ($D = k \times \lambda/\beta \times \cos\theta$, where D, k, λ, β, θ represent crystallite size, shape factor, wavelength of X-ray used, FWHM, and diffraction angle, respectively), CdS:La^{3+} HMSs have smaller crystallite size than CdS HMSs. The thickness of CdS:La^{3+} nanosheet unit measured through FE-SEM is smaller than that of undoped CdS nanosheet one (Fig.S4), which also supports the result of XRD analyses. Therefore, La^{3+} ion dopants could slightly inhibit the growth of CdS crystals in the reaction.The XRD peaks shifting to lower diffraction angle after doping can be understood by the lattice expanding as the result of doping larger La^{3+} ions (106 pm) on the Cd^{2+}ion (97 pm) sites of the CdS crystal lattice based on the Bragg's equation($2d\sin\theta = n\lambda$), which is consistent with previous dopant size-dependent XRD shift [23]. The HRTEM image of CdS:La^{3+} HMSs shows the lattice spacings of 0.358 nm and 0.316 nm, which agree with interplanar separation of (1 0 0) and (1 0 1) planes of hexagonal phase CdS, respectively (Fig. 1d). The EDX elemental mapping shows that La^{3+} ions were doped into CdS lattices (Fig. 1e). The ICP measurements indicates 3 % molar concentration of La^{3+} ions doped in CdS:La^{3+} HMSs, which implies that near all La^{3+} ions were doped into CdS HMSs.

XPS survey spectra indicate that the surface composition of CdS HMSs mainly consist of Cd and S elements, and Cd, S, La, C, and O elements for CdS:La^{3+} HMSs (Fig. S5a), respectively. The small quantity of C and O present in CdS:La^{3+} HMSs probably comes from adventitious carbon and chemisorbed oxygen [24]. Quantitative calculations of XPS data shows the molar percentage of La^{3+} ion in CdS:La^{3+} HMSs is *ca.* 2.5 %, which indicates that while some La^{3+} ions are doped inside the CdS lattice, most of the dopants are located at the surface or near the surface of CdS HMSs considering a total 3 % La^{3+} doping concentration. The binding energies of Cd 3d (Fig. S5b)and S 2p (Fig. S5c) for CdS HMSs are consistent with

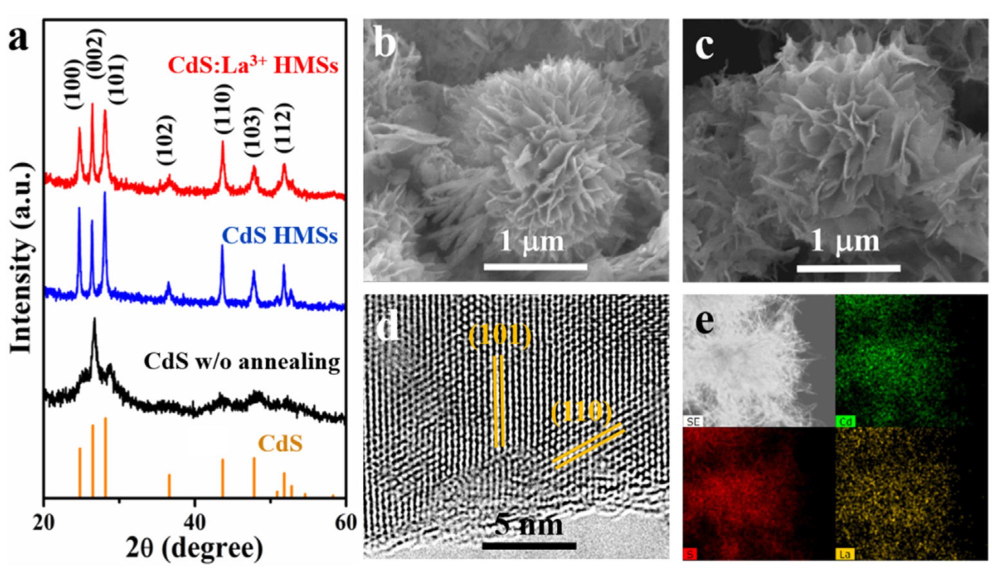

Fig. 1. XRD patterns of CdS synthesized through solvothermal route, CdS HMSs and CdS:La^{3+} HMSs after thermal annealing (a). FE-SEM images of CdS HMSs (b) and CdS:La^{3+} HMSs (c) after annealing. HRTEM image (d) and elemental mapping (e) of CdS:La^{3+} HMSs. Green, red, and yellow represent Cd, S, and La elements, respectively. (For interpretation of the references to colour in this figure legend, the reader is referred to the web version of this article.)

those of Cd and S in CdS [25]. The binding energies of Cd 3d3/2 and 3d5/2 are positively shifted by 0.09 eV after La^{3+} ions were doped into CdS, while those of S 2p are negatively shifted by 0.09 eV. This result shows that La^{3+} ions are doped into CdS crystal lattice and lead to charge redistribution of Cd and S. The binding energies of La 3d are located at 835.4 eV (La 3d5/2), 838.9 eV (La 3d5/2), 852.2 eV (La 3d3/2), and 855.7 eV (La 3d3/2) (Fig. S2d), which are closer to those of La 3d in $CdLa_2S_4$ rather than La_2S_3 [26,27]. The above XRD, EDX, and XPS results could confirm that La^{3+} ions were efficiently doped into CdS lattice.

UV–visible absorption spectra of pristine CdS HMSs and CdS:La^{3+} HMSs (Fig. 2a) indicate that the optical absorption edge of CdS was slightly blue shifted after La^{3+} ion doping. The band gap energy determined through $(\alpha h\upsilon)^2$ versus hυ curves increased from 2.25 eV to 2.34 eV after doping (inset in Fig. 2a). The slightly widened band gap mainly originates from the decreased crystal size of CdS:La^{3+} HMSs [16]. To ascertain the influence of La^{3+} ion doping on energy position of CdS HMSs, UPS of CdS and CdS:La^{3+} HMSs were measured (Fig. 2b and Fig. 2c). The work functions are 4.18 and 4.20 eV for CdS and CdS:La^{3+} HMSs, respectively, obtained through subtracting the secondary electron cut-off energy from the incident ultraviolet photon energy (He I excitation line, 21.22 eV). Therefore, their Fermi levels (E_F) are − 4.18 eV and − 4.20 eV versus vacuum energy level, respectively. The difference between E_F and valence band maximum (E_{VBM}) of CdS HMSs and CdS:La^{3+} HMSs are estimated to be 1.84 eV and 1.64 eV, respectively. Therefore, their E_{VBM} are − 6.02 eV and − 5.84 eV versus vacuum energy level. The calculated conduction band minimum (E_{CBM}) versus vacuum energy level of CdS and CdS:La^{3+} HMSs are − 3.77 eV and − 3.50 eV, respectively, using the equation $E_{CBM} = E_{VBM} + E_g$. To clearly show the positional relationship of their E_{CBM} and reduction potentials of CO_2 to CO and CH_4, energy band position changes of CdS HMSs before and after La^{3+} ion doping were further converted to normal hydrogen electrode potential (E_{NHE}) as shown in Fig. 2d. Obviously, both E_{CBM} and E_{VBM} of CdS HMSs were upshifted after the doping of La^{3+} ions. In theory, both CO and CH_4 can be thermodynamically produced on CdS HMSs and CdS:La^{3+} HMSs because of their more negative E_{CBM} than reductive potential of CO_2 toward CO and CH_4.

3.2. Visible-light-driven CO_2RR properties

To evaluate the influence of La^{3+} dopants on the photocatalytic properties of CdS HMSs, photocatalytic CO_2RR on CdS HMSs and CdS:La^{3+} HMSs were carried out under visible light irradiation (λ > 420 nm). It was found that both CdS HMSs and CdS:La^{3+} HMSs enable the photocatalytic reduction of CO_2 toward CO and CH_4 generation without any other liquid or gaseous CO_2 reduction products detected. Both the yields of CO and CH_4 were increased for CdS HMSs and CdS:La^{3+} HMSs with prolonging light irradiation time (Fig. 3a and 3b). However, La^{3+} ion doping significantly decreased the yield of CO but enhanced that of CH_4. Specifically, the mole percentage of CH_4 in the gaseous products increased from 46 % to 74 % within a 6-hour reaction time. The CH_4 selectivity (S_{CH4}) was further calculated based on the photoelectrons participating the CO_2-RR through the following equation:

$$S_{CH4} = 8R_{CH4}/(2R_{CO} + 8R_{CH4})$$

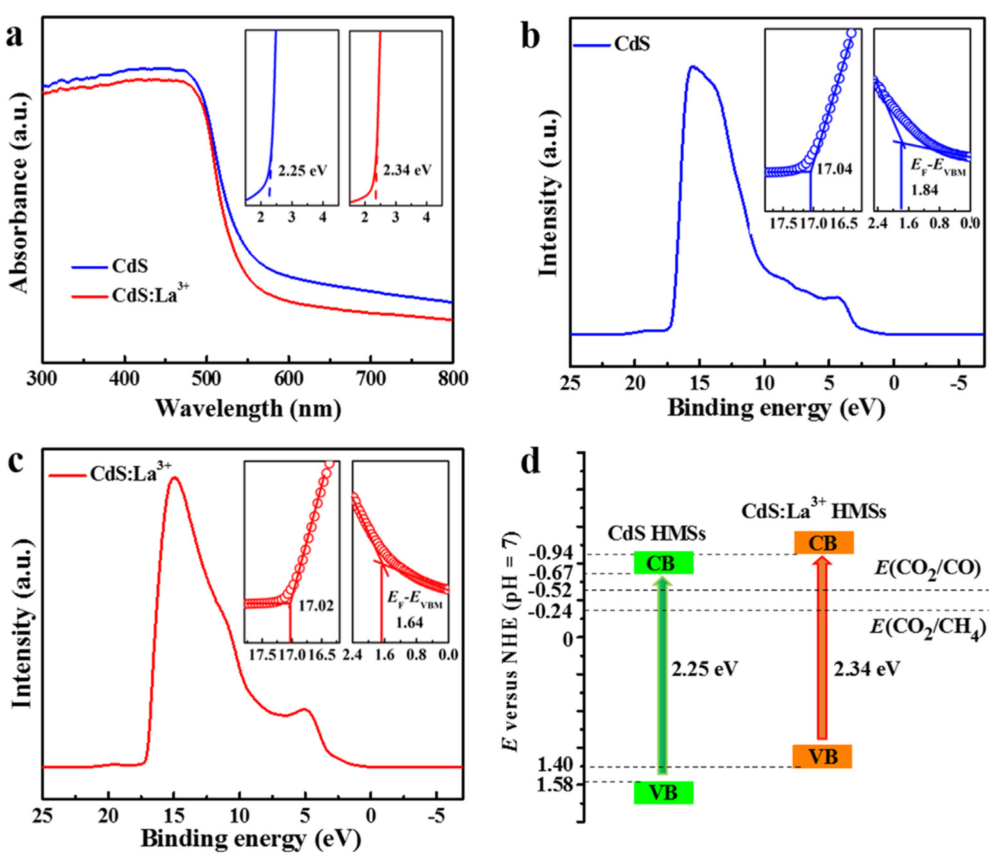

Fig. 2. UV–Vis absorption spectra (a) and corresponding curves of $(\alpha h\upsilon)^2$ versus hυ (the inset) of CdS HMSs and CdS:La^{3+} HMSs. UPS spectra and magnified views (the inset) for determining the secondary electron cut-off energy and E_{VBM} of CdS HMSs (b) and CdS:La^{3+} HMSs (c). Schematic illustration of energy band positions for CdS HMSs and CdS:La^{3+} HMSs, as well as reduction potentials of CO_2 to CO and CH_4 (d).

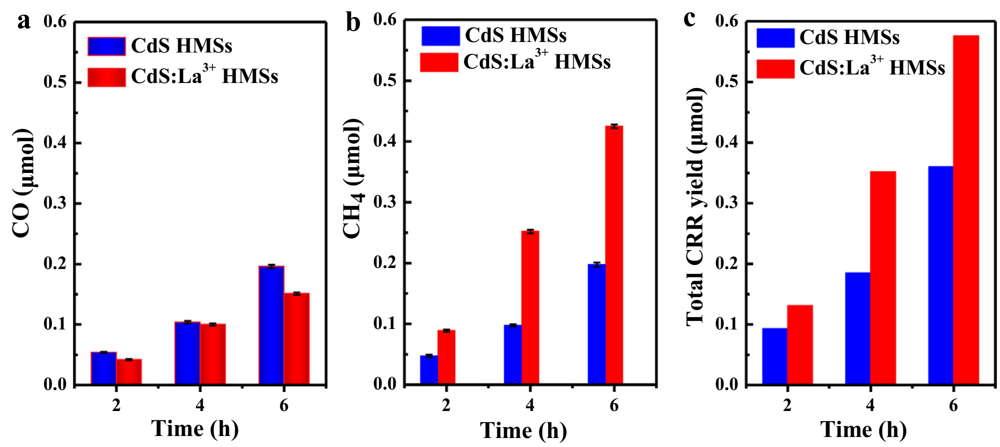

Fig. 3. CO (a), CH_4 (b), total CO and CH_4 (c) gases evolution amounts at different photocatalytic reaction times over CdS HMSs and CdS:La^{3+} HMSs. The error bars represent the standard deviation from three independent tests.

Where 8, 2, and R represent the consumed electron numbers of CO_2 reduction to CH_4 and CO and the formation rates of corresponding products, respectively. As a result, S_{CH4} of CdS:La^{3+} HMSs was increased from 77 % to 92 % due to La^{3+} ion doping, while no significant change in S_{CH4} was detected for both CdS HMSs and CdS:La^{3+} HMSs during photocatalytic CO_2RR processes (Fig. S6). Furthermore, the total amount of CO and CH_4 reaches 0.57 μmol for CdS:La^{3+} HMSs within 6 h under visible light irradiation, which is 1.7 times larger than that obtained over pristine CdS HMSs (0.33 μmol) (Fig. 3c). Therefore, La^{3+} ion doping can significantly enhance CH_4 production and selectivity, as well as boost the total photocatalytic CO_2RR activity. The apparent quantum yield of CH_4 could reach 1.4 % under monochromatic irradiation of 420 nm. In addition, the activity and CH_4 selectivity of photocatalytic CO_2RR for CdS:La^{3+} HMSs is the highest among the reported results to the best of our knowledge (Table S1).

It should be mentioned that no CO_2 reduction products were obtained in the absence of photocatalysts or in the dark, indicating that the CO_2RR was a light-driven photocatalytic process. Neither CH_4 nor CO were detected from control experiments in the absence of CO_2 with other reaction parameters unchanged. When CdS:La photocatalysts were dispersed into TEOA, CH_4 and CO were not detected under visible light irradiation, either. In addition, CH_4 and CO could also be produced in water without addition of TEOA. The above experimental results demonstrate that CH_4 and CO came from photocatalytic CO_2 reduction reaction over CdS:La.

To further evaluate stability of the CdS:La^{3+} HMSs for photocatalytic CO_2RR, cycle tests were operated. CdS:La^{3+} HMSs showed negligible drop in CO and CH_4 production yield after 6 consecutive cycles under visible-light irradiation, suggesting their good photocatalytic stability (Fig.S7). The crystal phase and morphology of CdS:La^{3+} HMSs can be maintained in the recycled photocatalysts, as shown in the XRD (Fig. S8) and FE-SEM analysis (Fig. S9). Furthermore, XPS spectra show almost no change in surface chemical states and compositions of the CdS:La^{3+} HMSs after six cycle tests (Fig. S10). The high stability of the doped CdS:La^{3+} HMSs is promising for large scale photocatalytic CO_2RR in industrial applications.

3.3. Mechanism of enhanced photocatalytic activity and selectivity

The introduction of La^{3+} ion could promote the separation of photogenerated carriers (electrons and holes) of CdS HMSs, as confirmed by their photocurrent and PL spectra. Compared with CdS HMSs, CdS:La^{3+} HMSs showed 1.5 times larger photocurrent under the same measurement conditions (Fig. 4a), which shows photogenerated electrons and holes were more efficiently separated over CdS:La^{3+} HMSs. Consistent with larger photocurrent, PL intensity of CdS:La^{3+} HMSs is significantly lower than that of CdS HMSs (Fig. 4b), which suggests more efficient separation of photogenerated charge carriers and less exciton recombination in CdS:La^{3+} HMSs. The EIS of CdS:La^{3+} HMSs show a smaller semicircular diameter than the undoped CdS HMSs (Fig. 4c), indicating smaller charge transfer resistance in the doped CdS:La^{3+} HMSs than the undoped CdS HMSs.The enhanced separation and transfer efficiency of charge carriers for CdS:La^{3+} HMSs can be attributed to the role of La^{3+} ions as a trapping center for photoexcited electrons [28].

To achieve highly efficient photocatalytic CO_2RR, the fixation and activation of CO_2 is a prerequisite. As seen from Fig. 4d, the amount of adsorbed CO_2 on the CdS:La^{3+} HMSs is higher than that of CdS HMSs despite similar Brunauer – Emmett – Tellr (BET) specific area of the two HMSs (Fig. S11). This result shows that the introduction of La^{3+} ions can activate the surface of CdS HMSs and facilitate the adsorption of CO_2, which is attributed to the stronger oxophilicity of La^{3+} ions than Cd^{2+} ions [29]. To further confirm the role of the oxophilic dopants on CO_2 adsorption, CO_2 temperature programmed desorption (TPD) measurements were conducted. CO_2 TPD profiles (Fig. S12) show a higher number of basic sites, corresponding with the La^{3+} dopant locations, and therefore higher adsorption capacity toward CO_2 from CdS:La^{3+} HMSs than CdS HMSs. Taken together, the enhanced photocatalytic CO_2RR activity of CdS:La^{3+} HMSs are mainly attributed to: 1) enhanced CO_2 adsorption from the oxophilic La^{3+} dopant ions; 2) increased charge separation and transfer after introducing La^{3+} ions into CdS crystal lattice.

The reduction potentials of CO_2 toward CO and CH_4 are – 0.52 and – 0.24 V versus normal hydrogen electrode, respectively. Because the doping of La^{3+} ions upshifted conduction band position of CdS HMSs, the CO formation would become more thermodynamically favored. In theory, CO_2 reduction toward CH_4 involves $8e^- + 8H^+$ process, which is less favored than the $2e^- + 2H^+$ reduction of CO_2 to CO in kinetics. Interestingly, it was found that the yield of CO decreased and correspondingly the yield of CH_4 increased for doped CdS:La^{3+} HMSs (Fig. 3b). The enhanced CH_4 selectivity observed in the doped CdS:La^{3+} HMSs is intriguing and could indicate that La^{3+} ion doping modulates the surface environment of the CdS HMSs photocatalysts and may change energy barriers associated with the CO and CH_4 formation pathways.

To elucidate the enhanced CH_4 selectivity of CdS:La^{3+} HMSs, density functional theory (DFT) calculations on Gibbs free energy

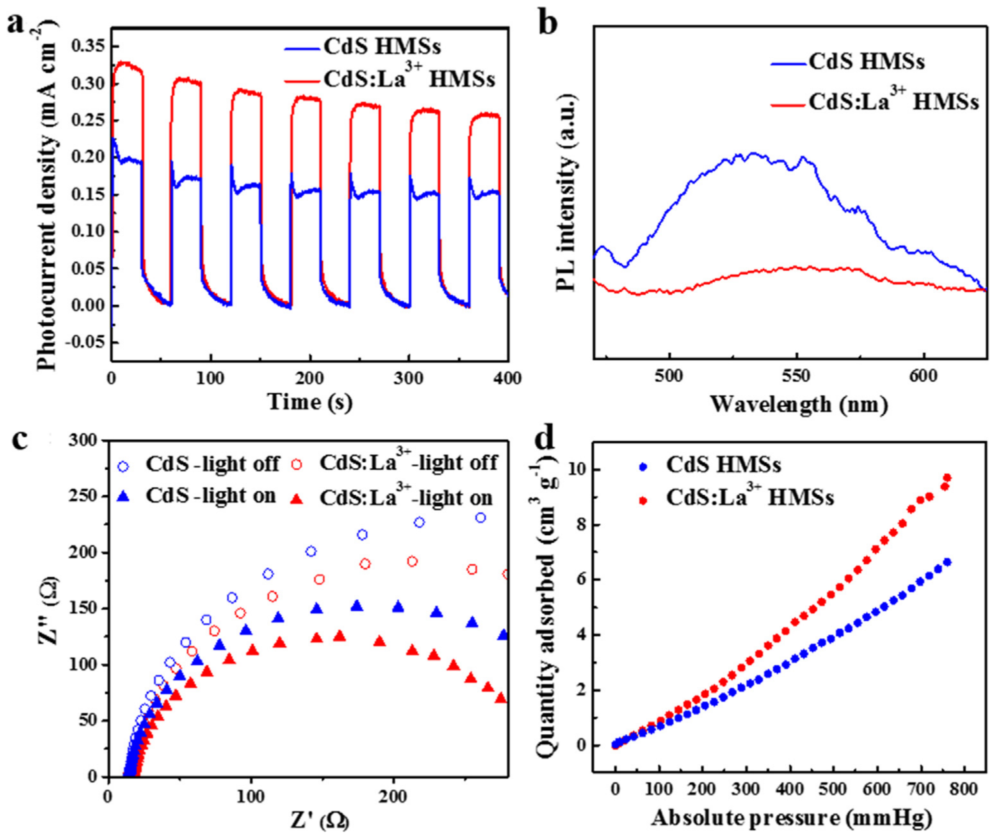

Fig. 4. Photocurrent spectra (a), PL spectra (b), EIS spectra in the dark and under visible light irradiation (c), and CO_2 adsorption isotherm curves (d) of CdS HMSs and CdS:La^{3+} HMSs.

of reaction pathways for CO and CH_4 formation from CO_2 reduction were carried out. As shown in Fig. 5a, the free energy of CO_2^* for doped CdS:La^{3+} is significantly lower than that of pristine CdS. This result suggests that the doping of La^{3+} ions can boost the CO_2 adsorption capacity of CdS HMSs, which is in good agreement with the results of CO_2 adsorption measurements (Fig. 4d). According to the calculations, the formation of CO* intermediate is the rate-limiting step for both photocatalytic CO_2RR toward CO over CdS HMSs and toward CH_4 over CdS:La^{3+} HMSs. The subsequent CO* conversion determines the products of the reaction, i.e., CO* direct desorption results in the production of CO, while further hydrogenation produces CH_4. Although the formation of CH_4 is an exothermic and spontaneous process for both photocatalysts, there is a significant difference in their reaction energy barriers for CO formation. The desorption energy barrier for CdS HMSs is 0.11 eV while CdS:La^{3+} HMSs have a much greater desorption energy barrier of 2.36 eV. The CO-TPD measurements (Fig. 5b) show that the CO desorption temperature for CdS:La^{3+} HMSs (202 °C) is higher than that of CdS HMSs (178 °C), which also supports the calculated results of CO desorption energy. The further hydrogenation of adsorbed CO* molecules into CHO* is much easier for CdS:La^{3+} HMSs than CdS HMSs due to the lower formation energy for the former than the latter. The result of CO-TPD measurements suggests that the doping of La^{3+} ion can activate adsorbed CO molecules, which can be supported by Bader charge analyses on CO adsorption structure. As shown in Fig. 5c, 0.15 e and 0.43 e were transferred from individual Cd sites in CdS HMSs and dual La and Cd sites in CdS:La^{3+} HMSs to the adsorbed CO molecules, respectively, indicating that adsorbed CO molecules can be easily activated on La sites. The stronger CO* adsorption and activation ability of La^{3+} ion than those of Cd^{2+} ions (Fig. 5a and 5b) is due to higher oxophilicity of the former than the latter. In addition, the desorption energy of CH_4 molecules on CdS:La^{3+} HMSs (−0.57 eV) is more negative than that on pristine CdS HMSs (−0.53 eV), which suggests that the CH_4 desorption from the surface of the former is also easier than that from the latter. This is possibly attributed to the strong adsorption of O in CH_3O^* on La^{3+} ions, which can weaken the C—O bands in CH_3O radical. As a result, the breakage of C—O bands and subsequent CH_4 desorption become more feasible. Considering all the above results, enhanced CH_4 selectivity for CdS:La^{3+} HMSs could be ascribed to the introduction of highly oxophilicity of La^{3+} ions on the surface of the CdS HMSs. Unreacted O* can be removed through TEOA acting as sacrificial agent freeing active sites for next catalytic cycle, which is supported by the fact that there is little change in surface oxygen content of CdS:La^{3+} HMSs after six cycle tests (Fig. S10).

In order to further confirm that La^{3+} ion doping could facilitate CO* hydrogenation to CH_4, in-situ DRIFT measurements over CdS and CdS:La^{3+} HMSs were carried out. To reduce the interference of organic TEOA molecules, only H_2O vapor and CO_2 gas were added into the sample cell. After 20 min adsorption of CO_2 gas and H_2O vapor over pristine CdS HMSs, as seen from Fig. 6A, some absorption bands assigned to bidentate carbonate species (b-CO_3^{2-}, located at 1650 and 1512 cm^{-1}), HCO_3^- (located at 1427 and 1215 cm^{-1}), and monodentate carbonate species (m–CO_3^{2-}, located at 1535, 1459, 1120,and 1088 cm^{-1}) are detected [30]. Under visible light irradiation, new vibration peaks corresponding to COO^- species (1337 cm^{-1}) and CH_3O^-groups (located at 1744 and 1706 cm^{-1}) appeared [31]. In contrast, after doping of La^{3+} ions, a new band appears at 1031 cm^{-1} (Fig. 6B) under visible light irradiation, which can be assigned to HCO* [32]. According to previous reports [33,34], $HCOO^-$ and COO^-species, HCO* and CH_3O^- groups

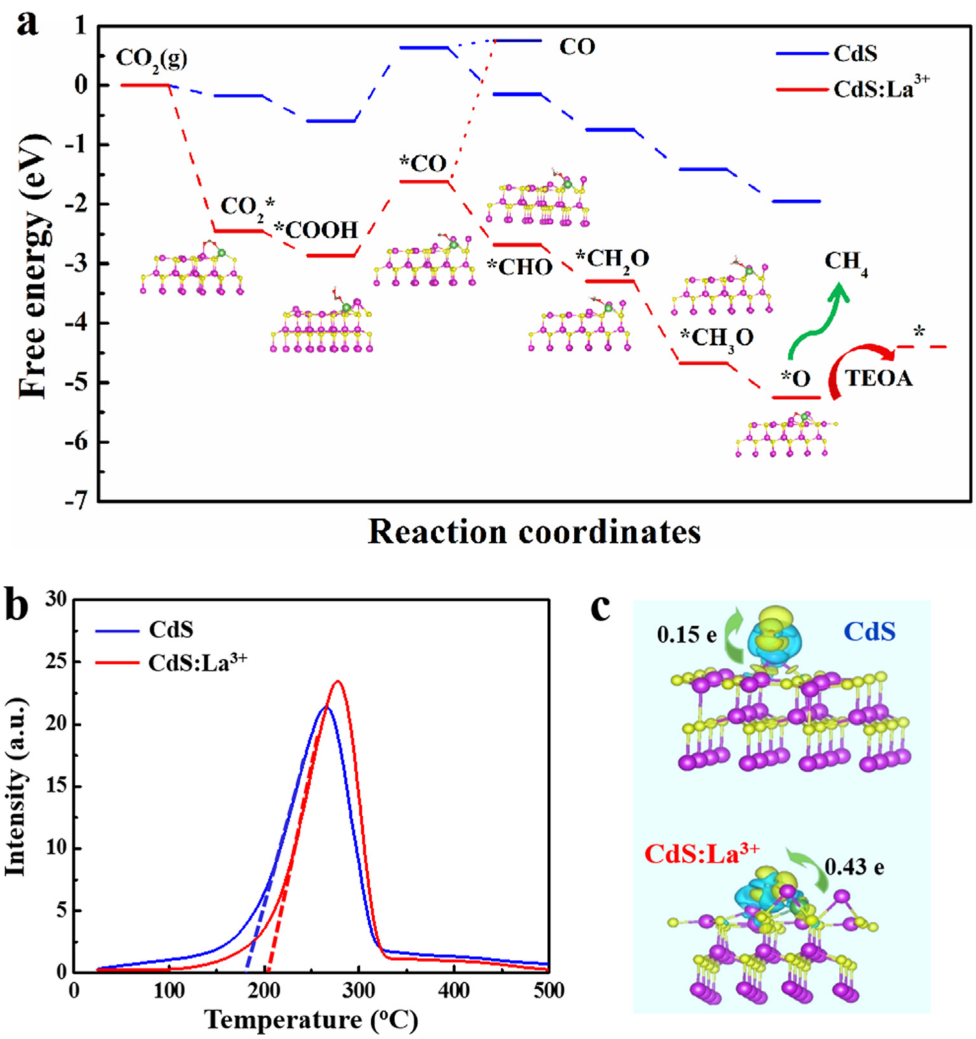

Fig. 5. Calculated Gibbs free energy diagrams for CO_2 reduction to CO and CH_4 over CdS and CdS:La^{3+} (a). CO-TPD profiles of CdS HMSs and CdS:La^{3+} HMSs (b). Charge density difference and net Bader charge transfer of CO adsorbed on Cd sites in CdS HMSs and dual Cd and La sites in CdS:La^{3+} HMSs (c).

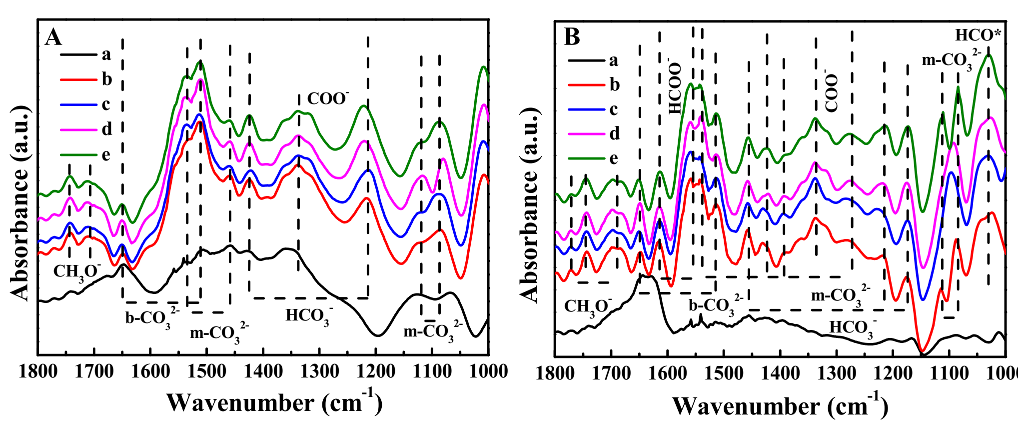

Fig. 6. In-situ DRIFT spectra of CdS HMSs (A) and CdS:La^{3+} HMSs (B) under different conditions: a) after flowing CO_2/H_2O gas for 20 min in darkness, b) visible light irradiation for 5 min, c) visible light irradiation for 10 min, d) visible light irradiation for 15 min, and e) visible light irradiation for 20 min.

are related to the important intermediate species in CO and CH_4 generation, respectively. The presence of strong HCO* signals from the doped HMSs indicates that the reaction paths of photocatalytic CO_2RR over CdS HMSs changed after La^{3+} ion doping. $HCOO^-$ and COO^- species were preferentially converted to HCO*, which is one of the intermediates for CH_4. Strong HCO* signal implies that more CH_4 will be produced on CdS: La^{3+} HMSs. In addition, the enhanced peak intensity ratio of CH_3O^- groups to COO^-species also indicates more CH_4 produced over CdS: La^{3+} than CdS. Therefore, in-situ DRIFTS data further approves that La^{3+} doping can change reaction pathways of photocatalytic CO_2RR and enhance CH_4 product selectivity of CdS HMSs.

To further confirm the role of the oxophilic surface of photocatalysts on the product selectivity in CO_2RR, we modulated the surface oxophilicity of a broad range of photocatalysts by introducing different dopants with different oxophilicity. To address the potential influence of doping concentration on CH_4 selectivity, we prepared the samples with different doping concentrations and the samples with optimal doping concentration were used for comparison. According to DFT calculations on a quantitative scale of oxophilicities θ(M) proposed by Kepp [29], θ values for La, Cd, and Au are 1.0, 0.2, and 0, respectively. As seen from the above photocatalytic CO_2RR results, CH_4 selectivity was enhanced after Cd^{2+} ions of CdS HMSs were partly replaced by La^{3+} ions with higher oxophilicity. On the contrary, when Au^{3+} ions with lowoxophilicity were doped in CdS HMSs (Fig. S13-17), the yield of CO significantly increased and reduced CH_4 production was observed (Fig. 7a). Specifically, CH_4 selectivity was decreased from 77 % to 59 % at the optimal doping concentration. This result is also consistent with reported single Au atom modified CdS and Ni^{2+} ion doped CdS that mainly produced CO during photocatalytic CO_2RR process [34,35].

Significantly, it was found that oxophilic La^{3+} ion doping is a general strategy to enhance activity and selectivity of photocatalytic CO_2RR toward CH_4 for various common photocatalysts such as ZnO nanoparticles (Fig. S18-20), SnS_2 nanosheets (Fig. S21-23), $BiVO_4$ hollow nanoplates (Fig. S24-26), BiOBr nanoplates (Fig. S27-29), TaON (Fig. S30-32), and $CsPbBr_3$ (Fig. S33-35) (Table S2). Furthermore, as seen from Fig. 8, the larger the positive oxophilicity difference between the dopant ion and the host metal element in the photocatalysts, the more significant enhancement in CH_4 selectivity was obtained (Table S3). It should be pointed out that enhanced CH_4 selective as the function of oxophilicity can also be abided by the samples with the same dopant concentration (Table S4-5, Fig. S39).If the metal ion in the host semiconductor photocatalyst has similar oxophilicity to that of La^{3+} ion, the La^{3+} ion doping only has a small effect on product selectivity. For example, La^{3+} doped TiO_2 (Fig. S36-38) showed similar product selectivity to that of pristine TiO_2 (Fig. 7b) due to the similar oxophilicity between La^{3+} and Ti^{4+}. However, for La^{3+} ion doped

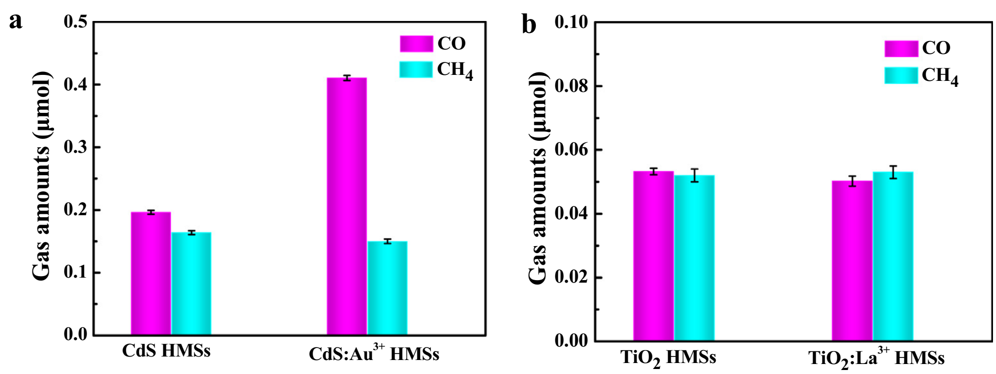

Fig. 7. CO and CH_4 gases evolution amounts over photocatalysts with different oxophilicity difference between the dopant ion and the host metal element under the optimal doping concentrations: CdS HMSs and CdS:Au^{3+} HMSs (a), TiO_2 and TiO_2:La^{3+} nanoparticles (b).

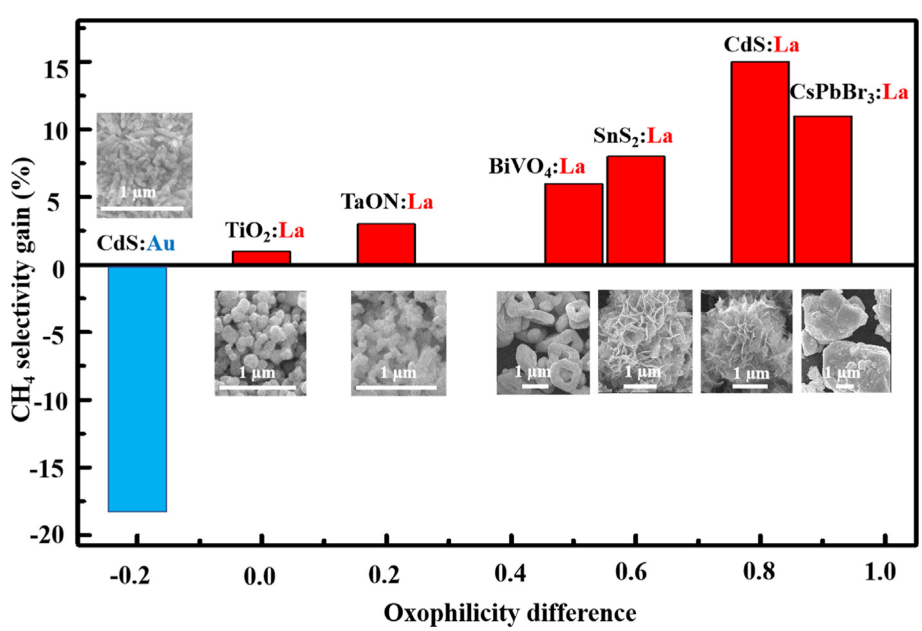

Fig. 8. The influence of oxophilicity difference between host metal elements and dopants in photocatalysts on CH_4 selectivity of CdS:Au, TiO_2:La, TaON:La, $BiVO_4$:La, SnS_2:La, CdS:La, and $CsPbBr_3$:La (from left to right). The insets show the SEM images of corresponding doped photocatalysts with the same order from left to right side.

CdS and $CsPbBr_3$ with larger oxophilicity differences between original metal sites and dopants (a difference of 0.9 between Pb and La and 0.8 between Cd and La), greater CH_4 selectivity was achieved (15 % for CdS:La^{3+} and 11 % for $CsPbBr_3$). The lower CH_4 selectivity gained for La^{3+} ions doped into $CsPbBr_3$ than that of CdS:La^{3+} might be due to the different bonding environments within the host lattice; especially considering the soft ionic nature of $CsPbBr_3$ (tested in pure organic phase, see Table S1 for details) [36], while CdS is largely covalent (tested in aqueous/organic phase). Further in-depth studies of the mechanism including the bonding, bandgap, size, and shape-dependent CH_4 selectivity are underway. However, the current results indicate that oxophilic doping is a general strategy to enhance CH_4 selectivity of photocatalytic CO_2RR. It is expected that more efficient photocatalysts with higher selectivity during CO_2RR could be developed through more elaborately designed oxophilic surfaces of the photocatalysts.

4. Conclusions

In summary, we have demonstrated that doping oxophilic La^{3+} ions increase both photocatalytic CO_2RR activity and CH_4 selectivity of the CdS HMSs photocatalysts. The enhanced photocatalytic CO_2RR activity of CdS:La^{3+} HMSs is attributed to improved photogenerated charge separation and transfer efficiency, as well as greater CO_2 adsorption capacity. Theoretical calculations indicate that the oxophilic La^{3+} ion dopants can 1) increase the energy barrier of CO* desorption and thus facilitate subsequent hydrogenation process, and 2) promote the breakage of C-O bands and the desorption of CH_4. As a result, higher CH_4 selectivity was achieved by the introduction of oxophilic La^{3+} ions to the CdS:La^{3+} HMSs. Furthermore, enhanced CH_4 selectivity can be achieved by doping oxophilic La^{3+} ions into various known photocatalysts such as ZnO, SnS_2, BiOBr, $BiVO_4$, TaON, and $CsPbBr_3$, demonstrating the general strategy to enhance CH_4 selectivity of photocatalytic CO_2RR through increased surface oxophilicity of the photocatalysts. The present study not only provides a new strategy for enhancing activity and selectivity of photocatalytic CO_2RR but also sheds light on the importance of surface oxophilicity engineering of the photocatalysts.

Data availability

No data was used for the research described in the article.

Declaration of Competing Interest

The authors declare that they have no known competing financial interests or personal relationships that could have appeared to influence the work reported in this paper.

Acknowledgements

This work was supported by the National Natural Science Foundation of China (No. 21673160 and 12075154) and startup funds of Shaoxing University. W.Z. acknowledges support from NSF CAREER (CHE-1944978) and NSF IUCRC Phase I grant(2052611).

Appendix A. Supplementary material

Supplementary data to this article can be found online at https://doi.org/10.1016/j.jcat.2022.10.004.

References

[1] C. Gao, J.X. Low, R. Long, T.T. Kong, J.F. Zhu, Y.J. Xiong, Heterogeneous single-atom photocatalysts: fundamentals and applications, Chem. Rev. 120 (2020) 12175–12216.

[2] J.W. Fu, K.X. Jiang, X.Q. Qiu, J.G. Yu, M. Liu, Product selectivity of photocatalytic CO_2 reduction reactions, Mater. Today 32 (2020) 222–243.

[3] T.T. Kong, Y.W. Jiang, Y.J. Xiong, Photocatalytic CO_2 conversion: What can we learn from conventional COx hydrogenation?, Chem Soc. Rev. 49 (2020) 6579–6591.

[4] Y.N. Wang, L.R. Winter, J.G.G. Chen, B.H. Yan, CO_2 hydrogenation over heterogeneous catalysts at atmospheric pressure: from electronic properties to product selectivity, Green Chem. 23 (2021) 249–267.

[5] M. Sayed, F.Y. Xu, P.Y. Kuang, J.X. Low, S.Y. Wang, L.Y. Zhang, J.G. Yu, Sustained CO_2-photoreduction activity and high selectivity over Mn, C-codoped ZnO core-triple shell hollow spheres, Nat. Commun. 12 (2021) 4936.

[6] X.D. Li, Y.F. Sun, J.Q. Xu, Y.J. Shao, J. Wu, X.L. Xu, Y. Pan, H.X. Ju, J.F. Zhu, Y. Xie, Selective visible-light-driven photocatalytic CO_2 reduction to CH_4 mediated by atomically thin $CuIn_5S_8$ layers, Nat. Energy 4 (2019) 690–699.

[7] S. Kreft, R. Schoch, J. Schneidewind, J. Rabeah, E.V. Kondratenko, V.A. Kondratenko, H. Junge, M. Bauer, S. Wohlrab, M. Beller, Improving selectivity and activity of CO_2 reduction photocatalysts with oxygen, Chem 5 (2019) 1818–1833.

[8] I. Shown, S. Samireddi, Y.C. Chang, R. Putikam, P.H. Chang, A. Sabbah, F.Y. Fu, W.F. Chen, C.I. Wu, T.Y. Yu, P.W. Chung, M.C. Lin, L.C. Chen, K.H. Chen, Carbon-doped SnS_2 nanostructure as a high-efficiency solar fuel catalyst under visible light, Nat. Commun. 9 (2018) 169.

[9] W. Gao, S. Li, H.C. He, X.N. Li, Z.X. Cheng, Y. Yang, J.L. Wang, Q. Shen, X.Y. Wang, Y.J. Xiong, Y. Zhou, Z.G. Zou, Vacancy-defect modulated pathway of photoreduction of CO_2 on single atomically thin $AgInP_2S_6$ sheets into olefiant gas, Nat. Commun. 12 (2021) 4747.

[10] S. Nitopi, E. Bertheussen, S.B. Scott, X.Y. Liu, A.K. Engstfeld, S. Horch, B. Seger, I. E.L. Stephens, K. Chan, C. Hahn, J.K. Norskov, T.F. Jaramillo, I. Chorkendorff, Progress and perspectives of electrochemical CO_2 reduction on copper in aqueous electrolyte, Chem. Rev. 119 (2019) 7610–7672.

[11] R. Subbaraman, D. Tripkovic, K.C. Chang, D. Strmcnik, A.P. Paulikas, P. Hirunsit, M. Chan, J. Greeley, V. Stamenkovic, N.M. Markovic, Trends in activity for the water electrolyser reactions on 3d M(Ni Co, Fe, Mn) hydr(oxy)oxide catalysts, Nat. Mater. 11 (2012) 550–557.

[12] B.E. Kahn, R.D. Rieke, Carbonyl coupling reactions using transition metals, lanthanides, and actinides, Chem. Rev. 88 (1988) 733–745.

[13] W.M. Wan, S.C. Ammal, Z.X. Lin, K.E. You, A. Heyden, J.G.G. Chen, Controlling reaction pathways of selective C-O bond cleavage of glycerol, Nat. Commun. 9 (2018) 4612.

[14] J. Wu, J. Liu, W. Xia, Y.Y. Ren, F. Wang, Advances on Photocatalytic CO_2 reduction based on CdS and CdSe nano-semiconductors, Acta Phys.-Chim. Sin. 37 (2021) 2008043.

[15] J.J. Wang, S. Lin, N. Tian, T.Y. Ma, Y.H. Zhang, H.W. Huang, Nanostructured metal sulfides: classification, modification strategy, and solar-driven C_O2 reduction application, Adv. Funct. Mater. 31 (2021) 2008008.

[16] G. Murtaza, S.M.A. Osama, M. Saleem, M. Hassan, N.R.K. Watoo, Structural, optical, and photocatalytic properties of $Cd_{1-x}S:La_x$ nanoparticles for optoelectronic applications, Appl. Phys. A 124 (2018) 778.

[17] G. Kresse, J. Hafner, Ab initio molecular dynamics for liquid metals, Phys. Rev. B 47 (1993) 558–561.

[18] G. Kresse, J. Furthmüller, Efficient iterative schemes for ab initio total-energy calculations using a plane-wave basis set, Phys. Rev. B 54 (1996) 11169–11186.

[19] J.P. Perdew, K. Burke, M. Ernzerhof, Generalized gradient approximation made simple, Phys. Rev. Lett. 77 (1996) 3865–3868.

[20] G. Kresse, J. Joubert, From ultrasoft pseudopotentials to the projector augmented-wave method, Phys. Rev. B 59 (1999) 1758–1775.

[21] P.E. Blöchl, Projector augmented-wave method, Phys. Rev. B 50 (1994) 17953–17979.

[22] J. Harl, L. Schimka, G. Jresse, Assessing the quality of the random phase approximation for lattice constants and atomization energies of solids, Phys. Rev. B 81 (2010) 115126.

[23] A. Davis, E. Hofman, K. Chen, Z.-J. Li, A. Khammang, H. Zamani, J.M. Franck, M. M. Maye, R.W. Meulenberg, W. Zheng, Exciton energy shifts and tunable dopant emission in manganese doped two-dimensional CdS/ZnS core/shell nanoplatelets, Chem. Mater. 31 (2019) 2516–2523.

[24] M. Stoev, A. Katerski, XPS and XRD study of photoconductive CdS films obtained by a chemical bath deposition process, J. Mater. Chem. 6 (1996) 377–380.

[25] D.W. Wakerley, M.F. Kuehnel, K.L. Orchard, K.H. Ly, T.E. Rosser, E. Reisne, Solar-driven reforming of lignocellulose to H_2 with a CdS/CdO_x photocatalyst, Nat. Energy 2 (2017) 17021.

[26] H. Liu, Z.Z. Xu, Z. Zhang, D. Ao, Highly efficient photocatalytic H_2 evolution from water over $CdLa_2S_4$/mesoporous g-C_3N_4 hybrids under visible light irradiation, Appl. Catal. B: Environ. 192 (2016) 234–241.

[27] S. Kaciuilis, A. Latisenka, A. Plesanovas, Rare-earth sesquisulphides investigation by ELS and XPS, Surf. Sci. 251–252 (1991) 330–335.

[28] A. Krukowska, M.J. Winiarski, J. Strychalska-Nowak, T. Klimczuk, W. Lisowski, A. Mikolajczyk, H.P. Pinto, T. Puzyn, T. Grzyb, A. Zaleska-Medynska, Rare earth

ions doped $K_2Ta_2O_6$ photocatalysts with enhanced UV-vis light activity, Appl. Catal. B: Environ. 224 (2018) 451–468.

[29] K.P. Kepp, A quantitative scale of oxophilicity and thiophilicity, Inorg. Chem. 55 (2016) 9461–9470.

[30] J. Baltrusaitis, J. Schuttlefield, E. Zeitler, V.H. Grassian, Carbon dioxide adsorption on oxide nanoparticle surfaces, Chem. Eng. J. 170 (2011) 471–481.

[31] L.B. Wang, B.C. Zhu, B. Cheng, J.J. Zhang, L.Y. Zhang, J.G. Yu, In-situ preparation of TiO_2/N-doped graphene hollow spherephotocatalyst with enhanced photocatalytic CO_2 reduction performance, Chin. J. Catal. 42 (2021) 1648–1658.

[32] J.T. Yates, R.R. Cavanagh, Search for chemisorbed HCO: the interaction of formaldehyde, glyoxal, and atomic hydrogen + CO with Rh, J. Catal. 74 (1982) 97–109.

[33] A. Singh, P. Verma, D. Samanta, A. Dey, J. Dey, T.K. Maji, 2D/2D/0D TiO_2/C_3N_4/Ti_3C_2 MXene composite S-scheme photocatalyst with enhanced CO_2 reduction activity, J. Mater. Chem. A 9 (2021) 5780–5786.

[34] Y.H. Cao, L. Guo, M. Dan, D.E. Doronkin, C.Q. Han, Z.Q. Rao, Y. Liu, J. Meng, Z. Huang, K.B. Zheng, P. Chen, F. Dong, Y. Zhou, Modulating electron density of vacancy site by single Au atom for effective CO_2 photoreduction, Nat. Commun. 12 (2021) 1675.

[35] J. Wang, T. Xia, L. Wang, X.S. Zheng, Z.M. Qi, C. Gao, J.F. Zhu, Z.Q. Li, H.X. Xu, Y.J. Xiong, Enabling visible-light-driven selective CO_2 reduction by doping quantum dots: trapping electrons and suppressing H_2 evolution, Angew. Chem. Int. Ed. 57 (2018) 16447–16451.

[36] A.H. Davis, W.W. Zheng, Discrete composition control of two-dimensional morphologic all-inorganic metal halide perovskite nanocrystals, J. Energy Chem. 59 (2021) 257–275.